

# High-Aspect-Ratio Nanoelectrodes Enable Long-Term Recordings of Neuronal Signals with Subthreshold Resolution

Pegah Shokoohimehr, Bogdana Cepkenovic, Frano Milos, Justus Bednár, Hossein Hassani, Vanessa Maybeck, and Andreas Offenhäusser\*

The further development of neurochips requires high-density and high-resolution recordings that also allow neuronal signals to be observed over a long period of time. Expanding fields of network neuroscience and neuromorphic engineering demand the multiparallel and direct estimations of synaptic weights, and the key objective is to construct a device that also records subthreshold events. Recently, 3D nanostructures with a high aspect ratio have become a particularly suitable interface between neurons and electronic devices, since the excellent mechanical coupling to the neuronal cell membrane allows very high signal-to-noise ratio recordings. In the light of an increasing demand for a stable, noninvasive and long-term recording at subthreshold resolution, a combination of vertical nanostraws with nanocavities is presented. These structures provide a spontaneous tight coupling with rat cortical neurons, resulting in high amplitude sensitivity and postsynaptic resolution capability, as directly confirmed by combined patch-clamp and microelectrode array measurements.

## 1. Introduction

One of the major challenges in modern neuroscience is to investigate information processing of neuronal networks with high spatio-temporal resolution and high signal-to-noise ratio (SNR). Although whole-cell patch-clamp and classic intracellular techniques excel in sensitivity, they are not apt for long-term and multiparallel recordings, due to their invasiveness and technical limitations. These challenges are surmounted by well-established planar multichannel devices, but at the

expense of signal-to-noise ratio. Without sufficient electrode–cell coupling, planar microelectrode arrays (MEAs) yield low amplitude signals that are challenging for spike sorting algorithms<sup>[1]</sup> to correctly attribute. The unresolved subthreshold signals cause loss of valuable information, essential to the direct estimation of synaptic weights and proper construction of connectivity matrices in neuronal networks.<sup>[2]</sup> Moreover, the highly sensitive parallel recordings would immensely support the rapidly growing field of neuromorphic engineering, yet again through accurate estimations of effective connectivity between the neurons.<sup>[3]</sup> In essence, there is a high demand for improvement of SNR and stable, parallel recording at postsynaptic potential (PSP) resolution. During the past decades, many electrode designs have been improved to achieve


this goal, resulting in intracellular access with a high yield and spatial resolution.<sup>[4]</sup>

To yield better cell–electrode coupling, numerous vertical nanostructures and nanoelectrodes have been developed by several groups.<sup>[5–13]</sup> In particular, it has been shown that sharp-edged,<sup>[14,15]</sup> high aspect (>10) ratio structures<sup>[9,16–19]</sup> display a high potential for complete membrane engulfment or even in-cell penetration,<sup>[20–23]</sup> resulting in an enlarged recorded signal.<sup>[11]</sup> An alternative strategy for promoting SNR aims at reduction of electrode impedance, and consequently noise. To minimize electrode impedance while preserving high spatial resolution, a wide range of materials have been implemented, such as IrO<sub>x</sub>,<sup>[24]</sup> TiN,<sup>[25]</sup> PtB,<sup>[4]</sup> and poly (3, 4-ethylenedioxythiophene): poly (4-styrenesulfonate) (PEDOT: PSS).<sup>[26,27]</sup> Yet another approach is the introduction of nanocavities between the sensing pads and passivation layer.<sup>[28,29]</sup> This increase in effective electrode area reduces impedance without increasing the electrode opening and therefore not impairing the spatial resolution of the array.

Even with such advances, securing a stable and long-term recording with PSP resolution remains a major challenge. Namely, while there is an indication of PSP detection solely as a result of a tight engulfment or penetration,<sup>[6,30,31]</sup> the majority of subthreshold recordings utilize electroporation<sup>[4]</sup> or optoporation,<sup>[12]</sup> which provide an intracellular access for a limited amount of time. Among those, only the active poration recordings have been confirmed by simultaneous patch-clamp.<sup>[24]</sup>

P. Shokoohimehr, B. Cepkenovic, F. Milos, J. Bednár, H. Hassani, V. Maybeck, A. Offenhäusser  
Institute of Biological Information Processing: Bioelectronics (IBI-3)  
Forschungszentrum Jülich GmbH  
Wilhelm-Johnen-Straße 1, 52428 Jülich, Germany  
E-mail: a.offenhaeusser@fz-juelich.de

P. Shokoohimehr, B. Cepkenovic, F. Milos, J. Bednár, H. Hassani  
Faculty 1  
RWTH Aachen University  
Templergraben 55, 52062 Aachen, Germany

 The ORCID identification number(s) for the author(s) of this article can be found under <https://doi.org/10.1002/smll.202200053>.

© 2022 The Authors. Small published by Wiley-VCH GmbH. This is an open access article under the terms of the Creative Commons Attribution-NonCommercial-NoDerivs License, which permits use and distribution in any medium, provided the original work is properly cited, the use is non-commercial and no modifications or adaptations are made.

DOI: 10.1002/smll.202200053

However, active poration has disadvantages in studying native behavior of neuronal networks. For example, simultaneous patch-clamp recordings during and after electroporation demonstrated an accompanying, non-negligible and sustained, membrane depolarization,<sup>[24]</sup> which may interfere with firing dynamics.

Here, we incorporate the concept of nanocavity (NC) MEAs with vertical nanostraws. High aspect ratio nanostraws (NS) were engineered to initiate tight cell–structure coupling, while the nanocavity reduces the electrode impedance. With the combination of microscopy and molecular biology, we found that this combination yields a spontaneous tight mechanical coupling. As a result, we acquired long-term recordings with increased signal amplitude, with no poration-inducing external forces or surface functionalization. Moreover, simultaneous patch-clamp and MEA recordings of the coupled neuron directly demonstrated the capability of our device to record postsynaptic potentials. Here we show that PSP resolution persisted throughout the >1 h measurements, indicating a stable and long-term subthreshold amplitude sensitivity. To our knowledge, this is the first time nonporated MEA recordings could consistently be combined with patch-clamp to compare MEA detected PSPs to the ground truth.

## 2. Results and Discussion

### 2.1. Characterization of NS–NC MEAs and the Electrode–Neuronal Membrane Interface

The fabrication of NS was adapted from the works of Ma<sup>[32]</sup> and Xie<sup>[33]</sup> who used track-etched membranes as templates. Here, high-aspect-ratio (>10) nanostraws were fabricated on electron beam resist templates by depositing 30 nm of TiO<sub>2</sub> through a series of plasma enhanced atomic layer deposition (PE-ALD) steps (Figure S1, Supporting Information). The nanostraw height was defined by the resist thickness. The nanostraws were placed on the center of 64 MEA electrode openings (Au/Pt, 8×8 grids). Two nanostraw patterns were designed to achieve 2 μm pitch on electrodes with 6 or 10 μm diameter passivation opening (details in Figure S2, Supporting Information). For 10 and 6 μm diameter electrode openings, 9 and 5 nanostraws were produced, respectively (Figure 1a; and Figure S3, Supporting Information). We utilized chromium etchant solution to create a nanocavity between the Au/Pt electrode and the passivation layer as described previously.<sup>[34]</sup>

Scanning electron microscopy demonstrated that the nanostraws were strongly bound on the electrode surface and were stable despite high aspect ratio and various critical fabrication steps. A slight conical shape on top of the nanostraw resulting from E-beam exposure dose could enhance the seal resistance when interfacing neurons, as reported previously (Figure 1).<sup>[12,35]</sup> Highly controlled fabrication processes led to low variations of height and geometry of nanostraws (≈0.3%). We calculated the nanostraw height to be  $2.44 \pm 0.01$  μm (avg ± STD, 18 electrodes), while the inner and outer diameters were 100 and 160 nm, respectively. Electrochemical impedance measurements were performed to estimate the influence of nanocavity and nanostraws on 10 μm diameter platinum elec-

trodes. We investigated four different cases: planar electrode, nanocavity, nanostraws, on planar electrodes, and nanostraws on nanocavity (Figure S4, Supporting Information). The values presented below are average impedance with standard deviations measured at 1 kHz, calculated for 10 electrodes. As previously reported,<sup>[28,29,34]</sup> the nanocavity reduces the electrode impedance compared to the planar electrode ( $387.9 \pm 50.7$  vs  $699.9 \pm 54.1$  kΩ), similar to the impedance reduction from PtB<sup>[36–38]</sup> and TiN deposition.<sup>[39]</sup> Then, we demonstrate that the presence of nanostraws on nanocavities and flat electrodes yields similar values ( $323.5 \pm 73.6$  and  $668.2 \pm 41.5$  kΩ, respectively) to without nanostraws. Therefore, while nanocavity reduces the impedance in both cases, no significant changes were detected after the introduction of nanostraws ( $p > 0.05$ , two-tailed *t*-test). There was no difference in impedance of NS–NC electrodes with different openings (data not shown). This is unsurprising, since the cavity remains the main contributor to the electrode impedance reduction, and the cavity size remains effectively similar in either case.

To characterize the interaction between neuron and nanostraws, we utilized confocal microscopy and scanning electron microscopy/focused ion beam sectioning (SEM/FIB). We visualized filamentous actin using LifeAct-RFP in cortical neurons growing on nanostraws. Prominent F-actin accumulations formed in all neuronal domains (dendrites, soma, and axon) localized to the cells' contact with the straws. Neurites did not form suspended structures as observed for other pointed micro- and nanostructures.<sup>[40,41]</sup> We observed F-actin in ring-like structures at the base of the straws (Figure 1b,c), though the exact interaction in the tip of the straw remains ambiguous. Actin rings are capable of generating tension within the cytoskeleton and are seen in other processes when a cell grasps an object.<sup>[42]</sup> Strong fluorescence signals at the end of nanostraws due to the membrane curvature indicate a close contact between the cell membrane and nanostraws.<sup>[43,44]</sup> These membrane convolutions greatly increase the area of membrane interacting with the chip, even for an electrode with the same lateral area. SEM/FIB showed membrane deformation at a high resolution, as well as deformation of subcellular compartments (Figure 1d). Straws protrude into the cell for nearly their entire length, without areas of suspended cell membrane between straws. Though the shape of organelles may be deformed, their membranes appear intact, suggesting the straws to not injure structures such as the nucleus. Overall, both the cytoskeleton rearrangement and deformation of the plasma and nuclear membrane indicate tight engulfment.

### 2.2. Stable, Long Term, and Sensitive Recording with NS–NC MEAs

Measurements lasting from 5 min to 2 h were performed on chips containing 62 measuring electrodes. For electrophysiological recordings, 790 cells mm<sup>−2</sup> E18 rat cortical neurons were cultured on chips >14 days, as ensuring prominent spontaneous activity. Substrates were coated with PLL to promote neuron adhesion, and no further functionalization was applied. After the standard cleaning procedure, the chips were reused over several cultures, demonstrating a robust design. The noise

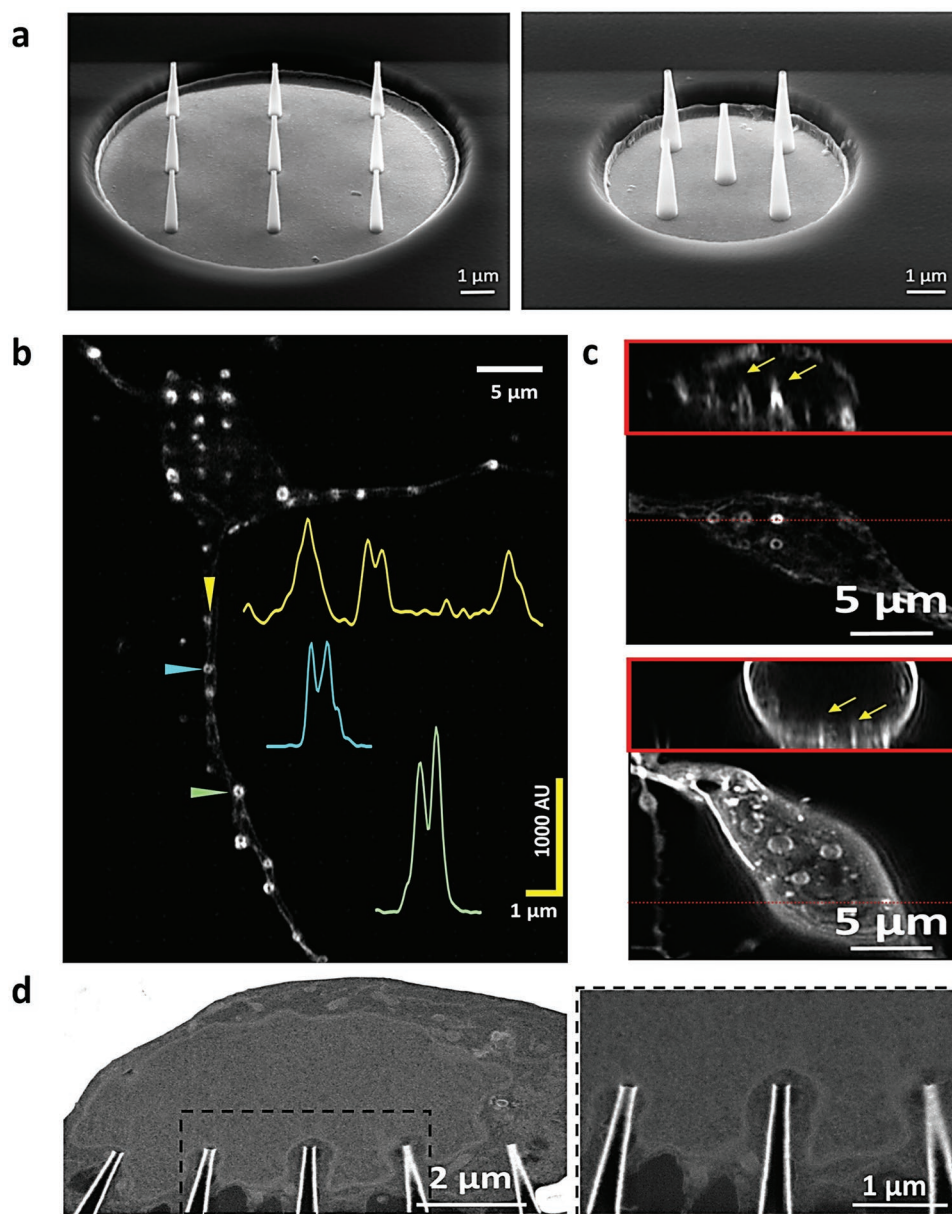


**Figure 1.** Characterization of nanoelectrodes and nanostraw-neuron interface. a) SEM images of the fabricated devices. Nanostraws with 2  $\mu\text{m}$  pitch on electrodes with 10  $\mu\text{m}$  diameter opening (left) containing 9 nanostraws and 6  $\mu\text{m}$  diameter opening (right) containing 5 nanostraws. b) Confocal microscopy visualizing neuron–nanostraw coupling. A neuron with soma in the top left interacts with straws in all compartments. Intensity profile plots along the directions indicated by colored arrows are shown in matching color on the right. All plots share the yellow scale bars. c) Top: The cytoskeleton forms actin-rich accumulations around the nanostraw (arrows). Bottom: The cell membrane is pushed upward by the nanostraws (arrows). The red panels in both micrographs represent orthogonal intensity projections of 30, 0.22  $\mu\text{m}$  slices at the position marked by the dotted line for a Lifeact-RFP-transfected neuronal cell (top) and a Dil-stained neuron (bottom) growing on nanostraws. d) High-resolution SEM/FIB of the neuron–nanostraw interface showing the nucleus deformed by the nanostraws.

level was determined as a root mean square (rms) error of the entire trace. Signals were identified when the trace exceeded three times the noise level, and their amplitudes were measured from peak to peak.

First, we present a typical 20 s recording of spontaneous neuronal activity at 18 days in vitro (DIV) (Figure 2a). Out of 62 recording channels, 37 were visibly contacted by somas or neurites (coupled electrodes), and 35 electrodes thereof have shown spontaneous network bursting events (Figure S5, Supporting

Information). Most of the channels are characterized by prominent spikes, with the average SNR of 16.5. The similar number of coupled electrodes and active channels per device, as well as the high average SNR indicate a high throughput capability and quality of our design. On the other hand, we demonstrate network burst events, well recognized in mature neuronal cultures grown on glass coverslips<sup>[45]</sup> and planar MEAs,<sup>[46]</sup> implying the biocompatibility and noninvasiveness of NS–NC MEAs. The average value of maximum SNR did not decrease for up to

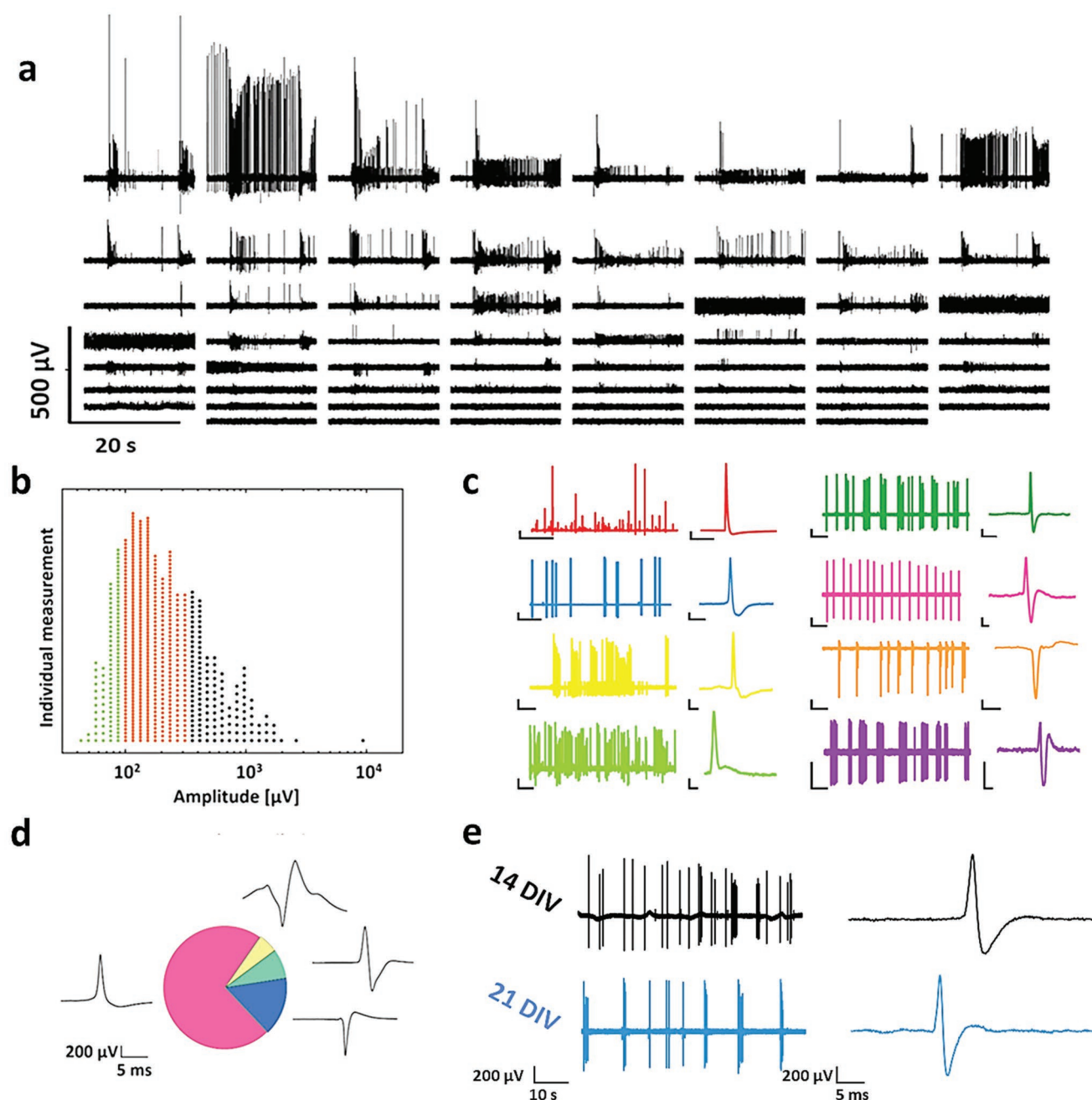


**Figure 2.** Signal characteristics from NS-NC MEA recordings. a) A representative recording from 62 recording channels of a single chip. Recordings are organized according to descending signal amplitude. b) Amplitude histogram of the highest peaks found in 693 active channels in 72 different samples. The color represents the amplitude ranges of distinct MEA designs: green dots, < 100  $\mu$ V, as in planar MEA signals, orange dots, 100–350  $\mu$ V, the range of nanocavity only MEAs, and black dots, >350  $\mu$ V spikes. c) MEA traces and exemplary APs from some of the channels with a highest amplitude signals. Scale bars enumerations removed for clarity; x-scale of all traces is 10 s, and for zoomed-in APs 5 ms. Y-scale is 200  $\mu$ V for both traces and APs, except for the red trace ( $y = 1$  mV). d) Incidence of waveforms in >500  $\mu$ V spikes calculated by K-means clustering followed by manual inspection. Bottom-left is a shared scale bar for average waveforms of each cluster. Pink (71.8%): positive monophasic signals; blue (15.5%): negative monophasic; green (7.7%): biphasic, yellow (5.1%): complex waveforms. e) Long-term recordings from the same channel, 1 min, at 14 DIV (black) and 21 DIV (blue).

10 consecutive cultures, further supporting the robustness and reusability of our design.

To estimate the long-term recording stability, we measured over consecutive days in culture. Figure 2e contains a representative recording from the same channel at 14 DIV (black)

and 21 DIV (blue); over the 7-day period, the activity changed from nonbursting to bursting behavior, a hallmark of network maturation, without a reduction in the channels with high signals as seen in transient poration measurements. This demonstrates that on NS-NC MEAs activity persisted and matured in

a similar trend reported on flat MEAs and glass coverslips. Furthermore, the simultaneous patch clamp experiments described below cover MEA measurements lasting over an hour, during which the waveform of both the MEA detected APs and sub-threshold signals remain stable (Figures S7 and S8, Supporting Information). This is  $\approx 10$  times longer than reported high signal amplitude due to poration.<sup>[4,8,14,24,47,48]</sup> One of the merits of NS-NC MEAs is the amplitude stability of the high signals (Figure 2e, right). This yet again shows that detected high signals do not arise due to the short-term changes, but are a consequence of a stable contact of the membrane and nanostraws.

To investigate the reproducibility of the fabrication process, we looked into the amplitudes in 693 active channels on 72 MEAs recorded over 12 neuronal preparations. With about 17% somal and 42% total cell material coverage area, on average, 16% of recording channels per chip showed neuronal activity (Figure S6, Supporting Information). The amplitude histogram in Figure 2b shows the highest amplitude detected for each active channel. Green circles represent low amplitude signals analogous to planar electrode recordings (40–100  $\mu\text{V}$ ).<sup>[49]</sup> The majority of assessed amplitudes (orange) falls into 100–350  $\mu\text{V}$  range, similar to nanocavity-only MEA recordings (previous unpublished results). However, 20% of the signal amplitudes surpassed the nanocavity only capability (black), with the maximum amplitude of 9 mV. Figure 2c shows about 1 min exemplary traces and AP waveforms from the channels containing some of the largest signals. In addition to positive monophasic spikes, negative, and biphasic spikes were also observed. Next, K-means clustering followed by manual curation of  $>500$   $\mu\text{V}$  signals, showed that 71.8% of high amplitude signals had a predominant positive component, 15.5% had dominant negative phase, 7.7% were biphasic, while 5.1% had complex waveforms (Figure 2d). Therefore, high amplitude signals are dominated by positive monophasic waveforms akin to the ones reported for in-cell recordings.<sup>[6]</sup>

In order to reveal the contribution of the structure to the signal quality, we designed planar electrodes with nanostraws and NS-NC MEAs with filled straws. Planar electrodes with nanostraws detected no signals above 100  $\mu\text{V}$ , which could be explained by the impedance of the planar MEAs. Filled nanostraws were created by omitting the electron beam resist removal. These samples test whether our structures serve exclusively as a scaffold to induce membrane curvature and tight engulfment, or if the signal travels through the nanostraws. Only 3% of active channels with filled nanostraws ( $N = 58$ ) showed signals above 800  $\mu\text{V}$  (maximum: 1735  $\mu\text{V}$ ). These experiments demonstrate the importance combined nanocavity-nanostraw to yield tight coupling and high SNR.

### 2.3. On-Chip Patch-Clamp Characterization of NS-NC MEA Signals

To further investigate the signals recorded with NS-NC MEA, we performed simultaneous patch-clamp and MEA recordings (Figure 3). Candidate neurons were selected from those situated near or on the electrodes that showed spontaneous activity up to 70 min prior to the patch-clamp experiments (Figure 3a; and Figure S8, Supporting Information). Current-clamp experi-

ments either allowed the recording of spontaneous neuronal firing (Figure 3b) or drove action potentials (APs) with current pulses (Figure 3c). In the former condition, negative current was applied to keep the recorded potential at the resting value of around  $-60$  mV, while in the latter, APs were triggered by a  $+300$  pA pulse (Figure 3c, green trace).

In presented recordings, each MEA recorded spike corresponded to the patch-clamp recorded AP (Figure 3; and Figure S7, Supporting Information). Along with APs, NS-NC MEAs detected accompanying subthreshold predepolarization, seen in spontaneous and induced APs (Figure 3). During the 250 ms stimulation pulses, the intracellularly detected baseline membrane potential shifted toward depolarized values, while the MEA electrode was not able to pick-up this prolonged depolarization. Since the MEA signal detection is primarily via capacitive coupling, the absence of sustained depolarization signal is expected. Additionally, both electrode capacitance and hardware-applied high-pass filter contribute to attenuation of current-evoked, sustained depolarization. The MEA waveforms fell between the intracellularly recorded AP and its first time derivative, indicating an experimental configuration closer to that previously reported for in-cell recordings (Figure 3b,c(iii)).<sup>[4,12,23]</sup> Patch-clamp acquired APs show an AP peak-to-peak amplitude (APA) of  $58.3 \pm 22.6$  mV and half-amplitude duration ( $\text{APD}_{50}$ ) of  $4.9 \pm 1.9$  ms, and corresponding MEA spikes had  $\text{APA} = 847.7 \pm 637.6$   $\mu\text{V}$  and  $\text{APD}_{50} = 2.6 \pm 1.1$  ms. Unsurprisingly, APA of intracellularly- and MEA-recorded spikes displayed a linear relationship, as did  $\text{APD}_{50}$  (Pearson's test:  $R = 0.98$ ,  $p < 0.001$ , and  $R = 0.69$ ,  $p < 0.001$ , respectively).

Next, we calculated the coupling coefficient as the mean amplitude ratio between MEA- and intracellularly recorded APs.<sup>[6]</sup> At  $\approx 1\%$ , it was estimated about 10x higher than that reported with planar MEAs.<sup>[6]</sup> As the coupling coefficient directly relates to the quality of the cell-electrode junction, we conclude that our high amplitude signals are, at least partially, a result of the high  $R_{\text{seal}}$ .<sup>[50–52]</sup> Therefore, we constructed a simple point-contact model to get a rough estimate of  $R_{\text{seal}}$ .

### 2.4. $R_{\text{seal}}$ Estimation

On-chip patch-clamp recordings of weakly coupled neurons were used to estimate the lower boundary of  $R_{\text{seal}}$ . The value of  $R_{\text{seal}}$  was estimated by clamping the intracellular voltage,  $V_{\text{in}}$ , to a predefined value (Figure 4) while recording the MEA signal,  $V_j$ .<sup>[53]</sup> When applying a voltage step to  $V_{\text{in}}$ ,  $V_j$  follows  $V_{\text{in}}$  at first, but then decays exponentially with the decay time  $\tau$ . According to the point-contact model  $V_j = V_{\text{MEA}}$ . Based on attenuated MEA responses in our coupled measurements, one can assume that  $\tau$  is dominated by the membrane capacitance of the junction,  $C_m^j$  and  $R_{\text{seal}}$ , ( $\tau = C_m^j \cdot R_{\text{seal}}$ ).<sup>[53]</sup> At the end of the voltage step, a second exponential response of  $V_{\text{MEA}}$  is observed. A simplified equivalent circuit schematic, valid for those DC transients, is given in Figure 4b.

Exponential fits to  $V_{\text{MEA}}$  were used to estimate  $R_{\text{seal}}$  by assuming a half spherical cell shape leading to  $C_m^j = \frac{1}{3} C_m$ , while the membrane capacitance  $C_m$  is determined through the patch-clamp experiment. An exemplary plot of  $V_{\text{MEA}}$  during stimulus onset and offset together with exponential fits is

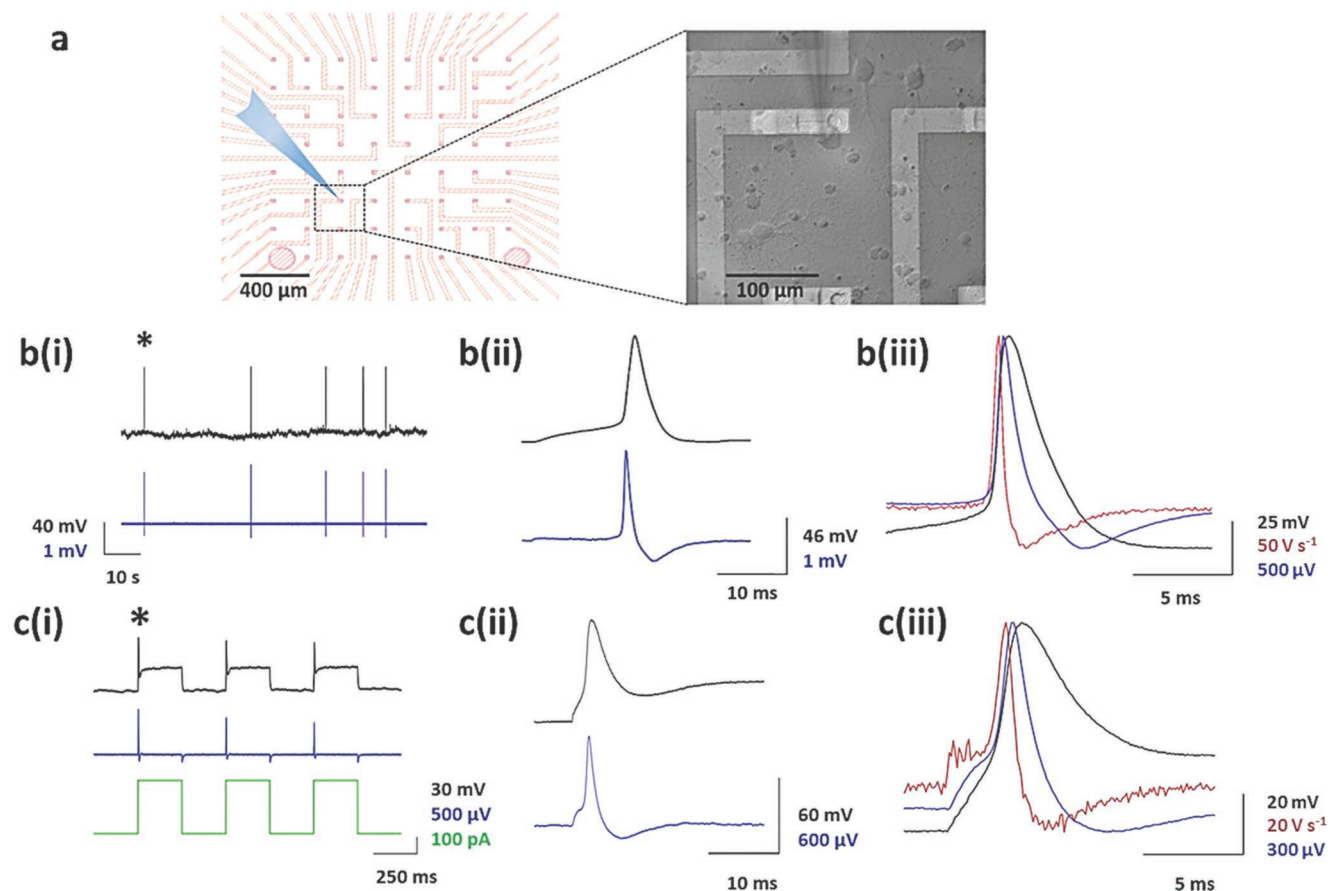


**Figure 3.** Combined somatic whole-cell patch-clamp and NS-NC MEA recordings. a) Left: schematic overview of on-chip patch-clamp experiments. Right: light micrograph of the patched neuron with soma positioned near a NS-NC electrode. b) Simultaneous patch-clamp (top black traces) and MEA recordings (bottom blue traces) of spontaneous activity and c) evoked APs during the current application through the patch pipette. b) Spontaneous activity (i) with zoomed in \*-ed spike (ii). B (iii): an overlay of average patch-clamp recorded APs (black), their first time derivative (red), and corresponding average MEA spikes (blue), from b (i). c) Simultaneous patch-clamp and NS-NC MEA recording of APs triggered by current pulses. (i) Triggered APs in patch-clamp (black), MEA (blue), and triggering pipette current (green). (ii) Focus on \*-ed AP showing prepolarization in both intracellular and MEA recording. (iii) Comparison of average triggered AP recorded by patch-clamp (black), MEA (blue), and the 1st time derivative of intracellular trace (red).

shown in Figure 4c.  $\tau$  are obtained between 0.5 and 2.5 ms, resulting in  $R_{\text{seal}}$  between 20 and 400 M $\Omega$ . While values for  $R_{\text{seal}}$  are clearly above the 10–20 M $\Omega$  reported for planar MEA recordings,<sup>[50]</sup> it must be noted that this is only a rough estimation of  $R_{\text{seal}}$  and that more details of the contact geometry are required for precise evaluation. As this approach assumes a cell-on-chip configuration where the cell membrane is not penetrated by the nanostraws, we demonstrate, that even in the absence of an in-cell recording, our NS-NC MEAs display a superior cell-chip-coupling.

## 2.5. NS-NC MEAs Record at Subthreshold Resolution

Simultaneous patch-clamp and MEA measurements of spontaneous neuronal activity confirmed that NS-NC electrodes can record subthreshold depolarizations. Out of 12 measurements of electrode-coupled neurons, the MEA electrodes detected PSPs in 7 (Figure S9, Supporting Information). Specifically, along with the high amplitude AP signals, smaller spikes matching

patch-clamp recorded PSPs were recorded (Figure 5a–d). These spikes persisted throughout the on-chip patch-clamp measurements lasting on average 15 min, and were also detected in the same channel prior the patch-clamp experiments (Figure S8, Supporting Information). The electrodes which detected PSPs had either positive monophasic or biphasic AP waveforms, with SNR ranging from 31.25 to 64.3. Pairing of patch-clamp detected PSPs and MEA signals was robust, suggesting these spikes represent PSPs and not signals from neighboring cells. It was also the case with quenched, coinciding PSPs, where distinct MEA spikes corresponded to individual events (Figure 5a bottom). Furthermore, NS-NC electrode displayed signals for PSPs, APs, and spikelets (Figure 5a right). EPSPs and IPSPs led to depolarization due to symmetric chloride concentration in the patch pipette and bath. Therefore, we could not differentiate between IPSPs and EPSPs in either recording.

MEAs also detected suprathreshold PSPs (Figure 5a), however, isolated, subthreshold events were used to characterize NS-NC MEAs' sensitivity. As seen from individual recordings (Figure 5a) and average waveforms (Figure 5b), the

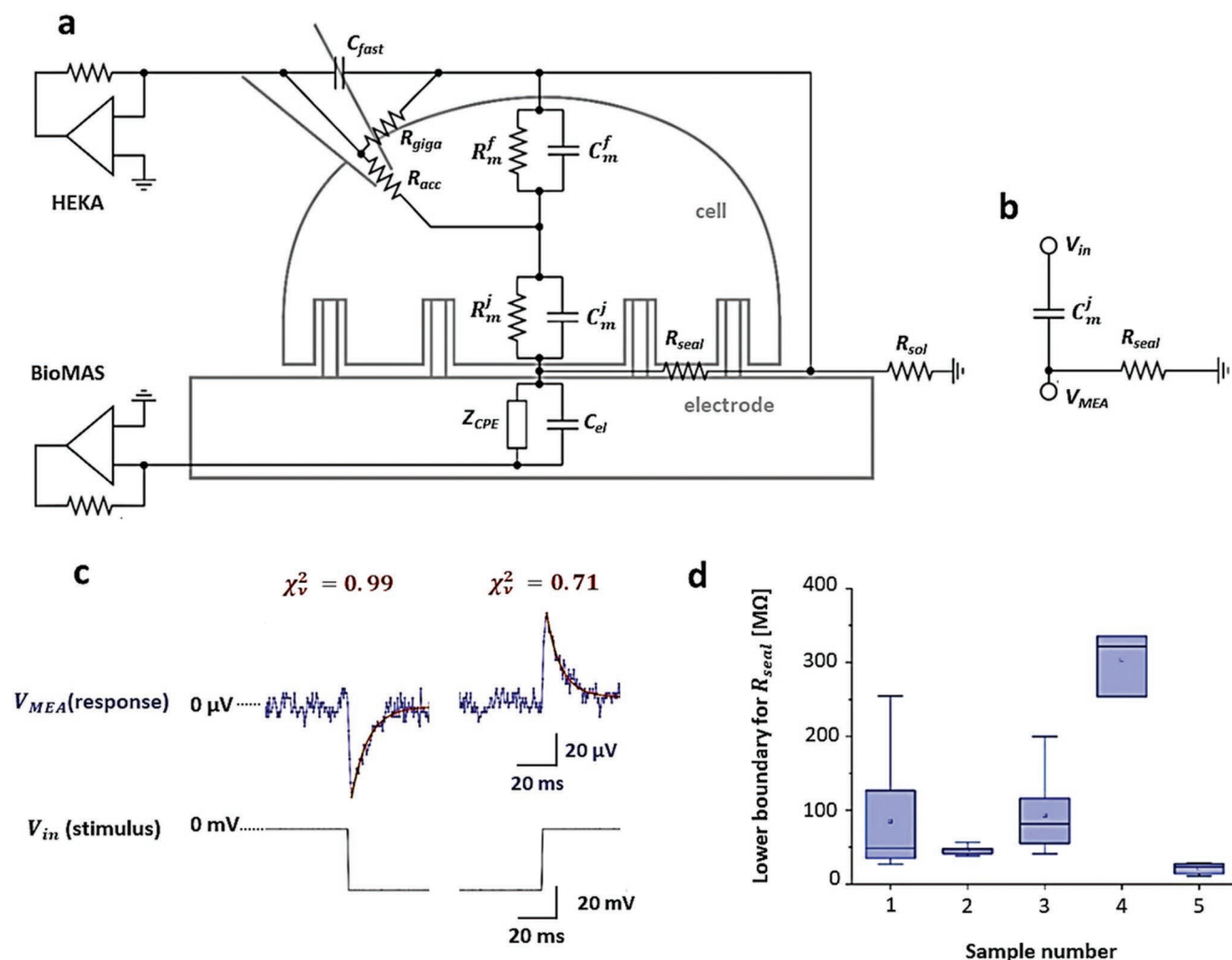


**Figure 4.**  $R_{seal}$  as a parameter for coupling quality. a) Electrical point-contact-model for a cell, forming a tight seal with a NS-NC-MEA, together with a patch pipette, used for intracellular stimulation and measurement. b) Equivalent circuit used for estimating  $R_{seal}$ . c) Voltage Clamp responses of MEA-signals at falling and rising edge of a negative patch clamp stimulus (sample 3 in d), exponential fits are indicated in red. d) Boxplot with values of  $R_{seal}$ .

chip-detected PSPs displayed a canonical monophasic shape with a steep rise and a prolonged, exponential decay. This decay was fit by a single exponential with a time constant  $\tau_{patch} = 34.24$  ms for intracellular recordings, while MEA-measured PSPs displayed nearly 10x faster decay,  $\tau_{MEA} = 3.61$  ms. Next, we calculated onset-to-peak amplitudes of PSPs. While the patch-clamp detected PSPs were  $18.8 \pm 9.1$  mV high, the chip-recorded PSPs were  $60.2 \pm 52.1$   $\mu$ V in amplitude (mean  $\pm$  SD). Furthermore, MEA PSP amplitudes cluster around the multiplies 21.8  $\mu$ V, pointing to the quantal nature of the synapses.<sup>[4]</sup> The intracellular and NS-NC recorded PSPs had a moderate, but statistically significant positive correlation of amplitudes (Pearson's test:  $R = 0.55$ ,  $p < 0.001$ ), further supporting NS-NC MEAs' detection of PSPs. For the measurement displayed in Figure 5, the PSP coupling coefficient was 0.32%, which was 3.8 times smaller than the AP coupling coefficient. The same trend persisted in other recordings of PSPs, with the PSP coupling coefficients ranging from 0.13 to 0.47, leading to coupling coefficients half to 1/5 that of corresponding APs (Table S6, Supporting Information). These results conflict the

present-day simulations that predict reduced signal attenuation in slower events.<sup>[6]</sup> The attenuation of low-frequency recordings might be the consequence of a dominant capacitive component of the coupling, as average MEA waveforms match the 1st time derivative of intracellular traces (Figure 5d). This reduction in coupling coefficient for subthreshold events likely prevents the NS-NC MEAs from detecting miniature postsynaptic events caused by stochastic vesicle releases, whose intracellular amplitude goes up to a millivolt.

In exceptional cases, NS-NC MEAs recorded events that did not match the intracellular trace in addition to intracellular APs (Figure S10, Supporting Information). These contaminations from neighbors could be distinguished straightforwardly, even from the MEA recordings only. As previously mentioned, mature neuronal cultures exhibit highly correlated network activity, and the electrodes recording from multiple neurons sporadically show complex merged waveforms, well-known to the spike-sorting community.<sup>[54]</sup> Second, the waveforms from neighboring neurons had shapes as reported in Figure 2, lacking the positive monophasic shape with exponential decay

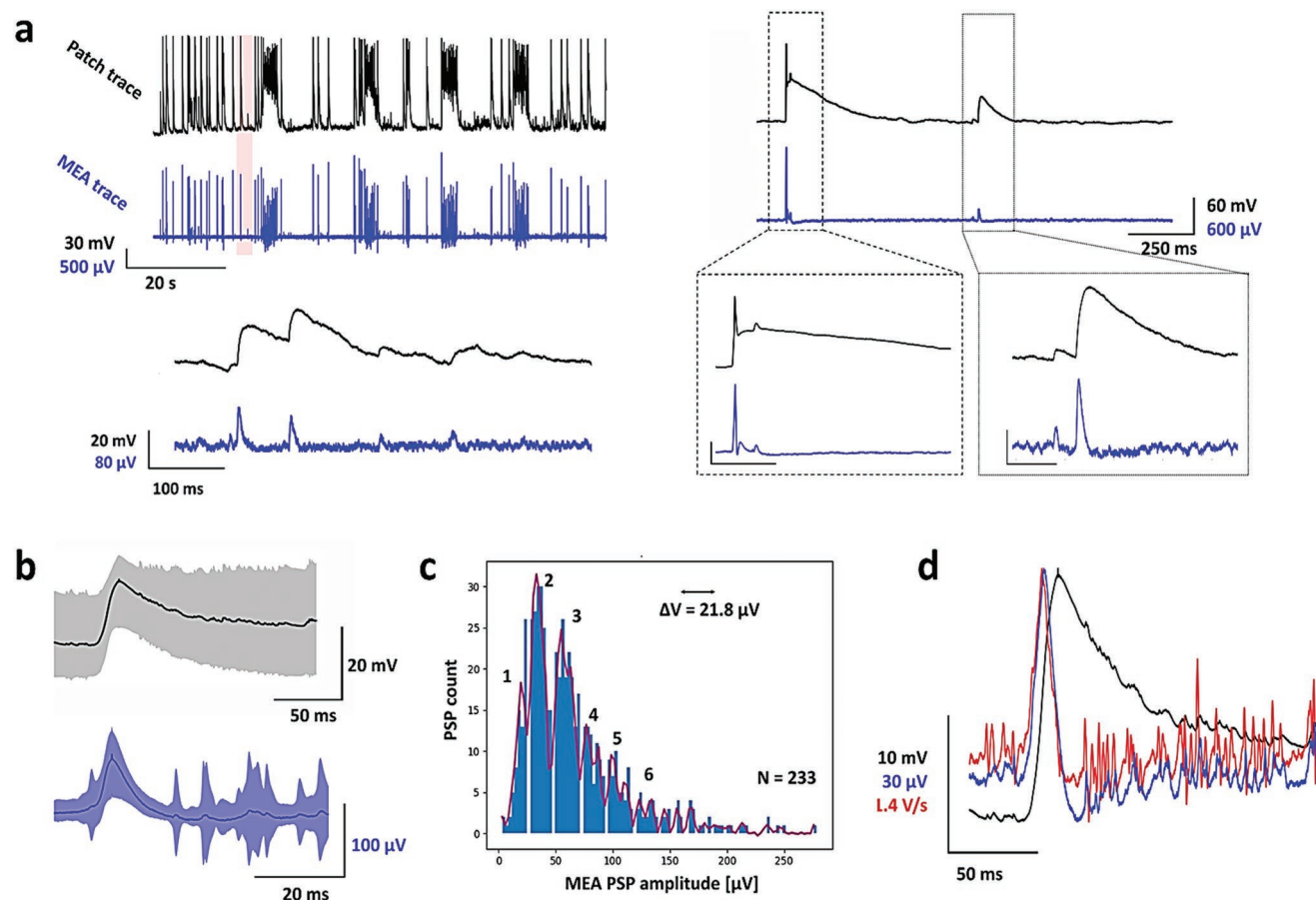


**Figure 5.** NS-NC MEAs record at subthreshold resolution confirmed by patch-clamp. a) Spontaneous activity containing an AP and PSP in intracellular (black) and NS-NC-MEA traces (blue). Top left: a minute and a half simultaneous recording of the neuron's spontaneous activity. Right: zoom-in on pink shaded area to focus on AP triggered by a giant EPSP (left), and a spikelet (right). Vertical scale bar corresponds to 40 mV (black) and 400  $\mu$ V (blue). Time scale = 50 ms. Dotted: zoom of 2 PSPs in both patch-clamp and MEA traces. Amplitude scale is 20 mV (black) and 100  $\mu$ V (blue). Time scale = 5 ms. Bottom left: NS-NC-MEA detects distinct spikes that correspond to quenched and coinciding PSPs. b) Average, peak-aligned waveforms of 233 isolated PSPs recorded by patch-clamp (top) and MEA (bottom) from the same neuron. Shaded areas represent standard deviation of the signals. Additional "peaks" in the standard deviation are due to the wide time window, which includes subsequent PSPs. Patch-clamp and MEA average PSP waveforms, note individual time scales. c) Amplitude histogram of MEA detected PSPs, pointing to the quantal nature of synapses. d) Aligned average waveform of intracellularly detected PSPs (black), its first time derivative (red), and average MEA signal (blue).

typical for PSPs. These observations, together with estimation of minimum SNR value for PSP detection, enabled us to create a robust framework for PSP discrimination in MEA recordings. We investigated the channels containing spikes with SNR >30, which also contained accompanying, smaller spikes. Signal shape matching the canonical PSP waveforms as confirmed by patch-clamp, and the lack of merging to form a complex waveform, supports our designation of those recordings as PSPs (Figure S9, Supporting Information). In turn, we estimated that around 18% of active channels detected putative PSPs ( $N = 10$  chips).

### 3. Conclusion

In this work, we present a new type of nanostructured electrode demonstrating significant progress compared to state-of-the-art microelectrodes. By combining vertical nanostraws and nanocavity-MEAs, low-noise, and large-amplitude recordings of APs

as well as subthreshold events were demonstrated. This high amplitude sensitivity persisted over several weeks in culture, suggesting that it develops from a stable, spontaneous mechanical coupling. NS-NC MEAs are a noninvasive platform particularly suitable for long-term neurophysiological experiments, as neurons show signs of typical activity maturation. The fabrication of nanostraws on nanocavity MEA can be reproduced with high precision on a wafer scale by using standard electron beam lithography and ALD processes. Compared to nanomushroom design from Spira et al., which is particularly suitable for acquiring IN-CELL recordings in nonmammalian neurons, NS-NC design provides a suitable platform for a tight engulfment by mammalian neurons. At this point, we speculate that the subthreshold sensitivity is based on the combination of the two nanostructures: in earlier studies we could observe that parts of the cell membrane creep into the nanocavity and result in a good sealing,<sup>[28]</sup> while studies of other groups showed that nanostraws with a high aspect ratio are particularly well suited to penetrate the cell membrane.<sup>[32]</sup> Imaging cells on NS-NC

electrodes supports tight contact and high membrane curvature interactions. In addition, combined electrophysiology measurements and the accompanying electrical coupling model suggest that the increase in sealing resistance contributes to the increase of coupling coefficient. Although detected PSPs imply a presence of intracellular access, imaging cells on NS–NC electrodes supports tight contact and high membrane curvature, but not the cell penetration. As mentioned above, we assume that the high membrane curvature increases the junctional membrane conductivity<sup>[6]</sup> and provides enough membrane leakiness to provide subthreshold resolution. Interestingly, the simultaneous measurements showed that the MEA recorded PSP waveform matches the 1st derivative of the corresponding intracellular signal, whereas the AP waveform falls between these two. It is unsurprising since these two events involve different membrane responses.

Compared to other high-aspect ratio vertical nanostructures, which yielded spikes up to 10 mV, NS–NC MEAs detected high signals were mostly around 1 mV in amplitude, with the highest of 9 mV (Figure 2). Nevertheless, we demonstrated long-term and stable PSP sensitivity which can only be improved with additional optimizations of NS–NC MEA design. We speculate that a further increase in nanostraw height could help the improvement of NS–NC MEA's performance. Although further optimization is certainly needed to increase the yield of high-resolution recordings of primary neurons, our results show the enormous potential of our approach and several appealing features to improve the quality of multisite electrophysiological recording technologies. The fabrication process of NS–NC MEAs can be integrated with high-density complementary metal oxide semiconductor (CMOS) MEAs<sup>[55,56]</sup> to further increase the spatial resolution and investigate signals at distinct neuronal compartments. This would allow better understanding of network connectivity, as well as signal integration at the single neuron level. In addition, we propose the combination of our approach with in vivo electrophysiology to map the neuronal circuit with high temporal resolution and voltage sensitivity.

## 4. Experimental Section

**Nanostraw Fabrication:** Nanostraws were developed according to the concept of the Melosh group.<sup>[17,32]</sup> Briefly, negative photo resist (nLOF 2020, 4000 rpm, 2.5  $\mu\text{m}$  thickness) deposited on planar 40 nm Au on Si or MEAs was patterned using electron beam lithography (Vistec EBPG 5000plus HS) leading to nanopoles with 2.4  $\mu\text{m}$  height and 100 nm inner diameter. Then, 30 nm thick  $\text{TiO}_2$  was deposited by PE-ALD at 130  $^\circ\text{C}$ , leading to a conformal coverage of the surface including the nLOF structures. The  $\text{TiO}_2$  was mask-less, anisotropically etched by plasma enhanced reactive ion etching with  $\text{CF}_4$  and  $\text{O}_2$  [RF power: 20 W, ICP-RF 300W, 12 sccm (standard  $\text{cm}^3 \text{ min}^{-1}$ ) of  $\text{CF}_4$ , 4 sccm of  $\text{O}_2$ , 0.005 mbar, 0.5 min]. Subsequently photoresist was removed by washing in acetone and isopropanol, rinsed with water, then oxygen plasma (200 W, 300 sccm, 3 min). The e-beam patterning was aligned to the electrode openings. In a final step, the sacrificial chromium layer is wet chemically etched by Cr etch solution No.1 from MicroChemicals GmbH. Finished chips were glued to a 4 mm high glass ring using PDMS to provide a culture area over the array.

**Cell Culture:** All experiments were performed in accordance with Landesumweltamt für Natur, Umwelt und Verbraucherschutz, Nordrhein-Westfalen, Recklinghausen, Germany, Number 81-02.04.2018.

A190. Before plating, the devices were soaked in ethanol (70%) for 30 s, rinsed in sterile deionized water and allowed to dry. If not stated differently, all chemicals were purchased from Sigma-Aldrich. Poly-L-lysine (PLL) (1 mL, 0.01 mg  $\text{mL}^{-1}$ ) in Hank's balanced salt solution (HBSS), was applied to each substrate for 1 h at room temperature, and then washed twice in HBSS. Isolation of primary cortical neurons from E18 Wistar rats was performed via enzymatic digestion in in trypsin-ethylenediaminetetraacetic acid (EDTA) (0.05%) (Life Technologies GmbH) for 10 min at 37  $^\circ\text{C}$ . The isolated cells were transferred to Neurobasal medium supplemented with B27 (1% (1%) (Thermo Fisher Scientific (Gibco)), L-glutamine ( $0.5 \times 10^{-3} \text{ M}$ ) (Thermo Fisher Scientific (Gibco)) and Gentamicin (0.05 mg  $\text{mL}^{-1}$ ) and seeded at 790 cells  $\text{mm}^{-2}$  on chips or 150 cells  $\text{mm}^{-2}$  on substrates utilized for microscopy. The cultures were incubated at 37  $^\circ\text{C}$  and  $\text{CO}_2$  (5%). The whole-medium change was performed around 2 h after plating, and half of the medium was exchanged twice per week. Devices were reused after incubation in trypsin-EDTA (0.05%), followed by cleaning in Tergazyme (1%) (Alconox) in ultrapure water for 5 min.

**Actin and Membrane Staining:** The F-actin marker Lifeact-RFP was introduced to visualize the cytoskeleton's response to nanostraws. Dissociated cells were transfected with Lifeact-RFP plasmid<sup>[57]</sup> using the Amaxa Rat Neuron Nucleofector Kit (Lonza). 3–5 million cells were resuspended in Nucleofector transfection solution (100  $\mu\text{L}$ ) and transferred into an Amaxa cuvette loaded with Lifeact-RFP cDNA plasmid (3–6  $\mu\text{g}$ ). The cells were transfected using the Amaxa Nucleofector device, program G-013. Immediately after transfection, a warm supplemented RPMI 1640 medium (1 mL) was added. Live cells were counted using a trypan blue exclusion assay. Alternatively, cells were incubated with 1,1'-Diocadecyl-3,3',3'-Tetramethylindocarbocyanine Perchlorate (DiI; Invitrogen) to visualize the cell membrane interacting with nanostraws. Neurons at DIV 4–8 were incubated with DiI ( $5 \times 10^{-6} \text{ M}$ ) in phosphate buffer saline (PBS) for 20 min at 37  $^\circ\text{C}$ , then washed three times with PBS. In both cases, cells were imaged at DIV4-8 using a 63x oil immersion objective on a confocal laser-scanning microscope, LSM 880 equipped with an Airyscan detector providing super resolution imaging with increased acquisition speeds. High-resolution Z-stacks were taken and processed in ZEN and ImageJ.

**SEM and FIB:** For SEM, a Zeiss Gemini 1550 with secondary electron and in-lens detectors was used. For nanostraws quality assessment, imaging was conducted at 10–20 kV acceleration voltage. The cell-nanostraw interface was visualized via SEM, following a glutaraldehyde (GA) fixation, staining, and resin embedding procedure, which has been previously established at our institute.<sup>[58]</sup> Here, a complementary dual beam system, containing both electron and ion beam (Helios NanoLab Dual-beam 600i, FEI) was used. To allow electric grounding, samples with fixed neurons on nanostraws were sputtered with a thin layer of platinum (15 mA for 35 s). SEM images were taken from top and at 52 $^\circ$  viewing angle, at 3 kV acceleration voltage. Electron beam-induced deposition (EBID) was used to deposit a 0.4  $\mu\text{m}$  thick layer of platinum on neurons to be sectioned. Then the sample was tilted by 52 $^\circ$  and an additional 0.4  $\mu\text{m}$  thick platinum layer was deposited by ion beam induced deposition (IBID) with a voltage of 30 kV and a current of 0.43 nA. A gallium ion beam of 0.2 nA milled the cross section, followed by polishing at 30kV and 0.08 nA. The fixed voltage of 3 kV was used with secondary and back scattered electron detectors.

**BioMAS Recording:** MEA recordings were performed on neurons over several successive days from DIV 14–24. A Ag/AgCl pellet electrode was immersed in the medium for grounding. When on-chip patch-clamp was carried out, culture medium was exchanged with extracellular patch solution. These experiments prevented further culturing of the MEA due to patch-clamp damage. All of the amplitudes presented were calculated from peak to peak. Maximum SNR was calculated as amplitude ratios of the highest signal and baseline RMS. MEA recordings were performed by a 64 channel amplifier with a head stage gain of 10.1 and the main amplifier gain of 10 or 100 connected to the high-resolution A/D converter (USB-6255 DAQ National Instruments), which was controlled by a LabView script. The readout from 64 channels was not multiplexed. Signals were sampled at 10 kHz, digitized at  $\pm 10 \text{ V}$  ADC range, and

both low-pass filtered at 7.2 and 8.8 kHz (depending of the gain of the main amplifier) and high-pass filtered at 72 Hz, to prevent signal aliasing and drift potentials, respectively. MATLAB and Python scripts coded at our institute were used for visualization and analysis of recorded data.

**On-Chip Patch-Clamp Experiments:** Whole-cell recordings of DIV 14–24 neurons on NS-NC MEAs were acquired by patch-clamp amplifier EPC10 USB (Heka Elektronik) coupled to the PatchMaster software (Heka Elektronik). Cells were visualized with an AxioScope (Carl Zeiss AG). EPC10 and BioMAS outputs were reciprocally connected to external channel recorders for simultaneous patch-clamp and MEA recording. To correlate patch-clamp and MEA signals, the patch-clamp amplifier received the MEA amplifier output from the specific channel. Patch-clamp experiments were performed in a bath solution composed of: NaCl ( $120 \times 10^{-3}$  M), KCl ( $3 \times 10^{-3}$  M),  $MgCl_2$  ( $1 \times 10^{-3}$  M),  $CaCl_2$  ( $2 \times 10^{-3}$  M), HEPES ( $2 \times 10^{-3}$  M), at pH = 7.3 adjusted with NaOH. Micropipettes were pulled from a fire-polished 1.5 mm borosilicate glass with a laser puller (P-2000, Sutter Instrument) and filled with pipette solution composed of: NaCl ( $2 \times 10^{-3}$  M), KCl ( $120 \times 10^{-3}$  M),  $MgCl_2$  ( $4 \times 10^{-3}$  M), HEPES ( $5 \times 10^{-3}$  M), EGTA ( $0.2 \times 10^{-3}$  M), MgATP ( $0.2028 \times 10^{-3}$  M), at pH = 7.3 adjusted with KOH. With this set of solutions, pipette resistance was 5–10 M $\Omega$ . Experimentally estimated liquid junction potential of +4 mV was not corrected for. After giga-seal formation, brief suction pulses were applied to rupture the membrane in the micropipette tip. The signal was sampled at 10 kHz and low pass filtered utilizing a Bessel filter at 10 kHz (filter 1) and 3 kHz (filter 2). In both voltage- and current-clamp mode, the holding potential was set at –60 mV. For voltage-clamp experiments, hyperpolarizing and depolarizing 500 ms pulses in the range between –120 and +100 mV were applied. Recordings were plotted and analyzed in a self-made Python script.

**Statistical Analysis:** A two-tailed t-test was performed to compare the impedances of NC and NS-NC MEAs. The chosen threshold for not-rejecting the null hypothesis was  $p = 0.05$ . Data were presented as (mean  $\pm$  SD) where indicated in the text. The amplitudes and widths of simultaneous patch and MEA signals were tested for correlation using Pearson's test, with the threshold of  $p = 0.001$ . Data were not normalized, outlier-filtered, or otherwise conditioned.

## Supporting Information

Supporting Information is available from the Wiley Online Library or from the author.

## Acknowledgements

P.S. and B.C. contributed equally to this work. The authors appreciatively thank M. Banzet for the production of MEA, S. Trellenkamp, F. Lentz, and E. Neumann for generous supports and advice on electron beam lithography, HNF staff for their kindly supports, and M. Prömpers for ALD support. The authors are grateful for the help of B. Breuer for the neuronal preparations. They would like to thank E. Brauweiler-Reuters for performing FIB/SEM. They also thank E. Savelyeva, T. Hondrich, K. Srikantharajah, and M. Alhaskir for valuable discussions during this work. This work was funded by the Helmholtz Association.

Open access funding enabled and organized by Projekt DEAL.

## Conflict of Interest

The authors declare no conflict of interest.

## Data Availability Statement

The data that support the findings of this study are available from the corresponding author upon reasonable request.

## Keywords

3D nanoelectrodes, microelectrode arrays (MEAs), neuron–electrode interfaces, postsynaptic potentials

Received: January 4, 2022

Revised: April 24, 2022

Published online: May 8, 2022

- [1] P. Stratton, A. Cheung, J. Wiles, E. Kiyatkin, P. Sah, F. Windels, *PLoS One* **2012**, 7, e38482.
- [2] D. A. Rusakov, L. P. Savtchenko, P. E. Latham, *Trends Neurosci.* **2020**, 43, 363.
- [3] D. Ham, H. Park, S. Hwang, K. Kim, *Nat. Electron.* **2021**, 4, 635.
- [4] J. Abbott, T. Ye, K. Krenek, R. S. Gertner, S. Ban, Y. Kim, L. Qin, W. Wu, H. Park, D. Ham, *Nat. Biomed. Eng.* **2020**, 4, 232.
- [5] A. Hai, J. Shappir, M. E. Spira, *Nat. Methods* **2010**, 7, 200.
- [6] M. E. Spira, A. Hai, *Nat. Nanotechnol.* **2013**, 8, 83.
- [7] X. Duan, R. Gao, P. Xie, T. Cohen-Karni, Q. Qing, H. S. Choe, B. Tian, X. Jiang, C. M. Lieber, *Nat. Nanotechnol.* **2012**, 7, 174.
- [8] C. Xie, Z. Lin, L. Hanson, Y. Cui, B. Cui, *Nat. Nanotechnol.* **2012**, 7, 185.
- [9] J. T. Robinson, M. Jorgolli, A. K. Shalek, M.-H. Yoon, R. S. Gertner, H. Park, *Nat. Nanotechnol.* **2012**, 7, 180.
- [10] F. Santoro, S. Dasgupta, J. Schnitker, T. Auth, E. Neumann, G. Panaitov, G. Gompper, A. Offenhäusser, *ACS Nano* **2014**, 8, 6713.
- [11] M. R. Angle, B. Cui, N. A. Melosh, *Curr. Opin. Neurobiol.* **2015**, 32, 132.
- [12] M. Dipalo, H. Amin, L. Lovato, F. Moia, V. Caprettini, G. C. Messina, F. Tantussi, L. Berdondini, F. De Angelis, *Nano Lett.* **2017**, 17, 3932.
- [13] B. Desbiolles, E. de Coulon, A. Bertsch, S. Rohr, P. Renaud, *Nano Lett.* **2019**, 19, 6173.
- [14] M. Dipalo, V. Caprettini, G. Bruno, F. Caliendo, L. D. Garma, G. Melle, M. Dukhinova, V. Siciliano, F. Santoro, F. De Angelis, *Adv. Biosyst.* **2019**, 3, 1900148.
- [15] H.-Y. Lou, W. Zhao, Y. Zeng, B. Cui, *Acc. Chem. Res.* **2018**, 51, 1046.
- [16] B. D. Almquist, N. A. Melosh, *Proc. Natl. Acad. Sci. USA* **2010**, 107, 5815.
- [17] X. Xie, A. M. Xu, S. Leal-Ortiz, Y. Cao, C. C. Garner, N. A. Melosh, *ACS Nano* **2013**, 7, 4351.
- [18] M. Dipalo, A. F. McGuire, H.-Y. Lou, V. Caprettini, G. Melle, G. Bruno, C. Lubrano, L. Martino, X. Li, F. De Angelis, *Nano Lett.* **2018**, 18, 6100.
- [19] D. Brüggemann, B. Wolfrum, V. Maybeck, Y. Mourzina, M. Jansen, A. Offenhäusser, *Nanotechnology* **2011**, 22, 265104.
- [20] A. M. Xu, A. Aalipour, S. Leal-Ortiz, A. H. Mekhjian, X. Xie, A. R. Dunn, C. C. Garner, N. A. Melosh, *Nat. Commun.* **2014**, 5, 3613.
- [21] O. Staufer, S. Weber, C. P. Bengtson, H. Bading, A. Rustom, J. P. Spatz, *Nano Lett.* **2019**, 19, 3244.
- [22] J.-H. Lee, A. Zhang, S. S. You, C. M. Lieber, *Nano Lett.* **2016**, 16, 1509.
- [23] N. Shmoel, N. Rabieh, S. M. Ojovan, H. Erez, E. Maydan, M. E. Spira, *Sci. Rep.* **2016**, 6, 27110.
- [24] Z. C. Lin, C. Xie, Y. Osakada, Y. Cui, B. Cui, *Nat. Commun.* **2014**, 5, 3206.
- [25] A. Stett, U. Egert, E. Guenther, F. Hofmann, T. Meyer, W. Nisch, H. Haemmerle, *Anal. Bioanal. Chem.* **2003**, 377, 486.
- [26] T. Someya, Z. Bao, G. G. Malliaras, *Nature* **2016**, 540, 379.
- [27] Y. Liu, A. F. McGuire, H.-Y. Lou, T. L. Li, J. B.-H. Tok, B. Cui, Z. Bao, *Proc. Natl. Acad. Sci. USA* **2018**, 115, 11718.
- [28] B. Hofmann, E. Kätelhön, M. Schottdorf, A. Offenhäusser, B. Wolfrum, *Lab Chip* **2011**, 11, 1054.
- [29] A. Czeschik, P. Rinklin, U. Derra, S. Ullmann, P. Holik, S. Steltenkamp, A. Offenhäusser, B. Wolfrum, *Nanoscale* **2015**, 7, 9275.

- [30] R. Liu, R. Chen, A. T. Elthakeb, S. H. Lee, S. Hinckley, M. L. Khraiche, J. Scott, D. Pre, Y. Hwang, A. Tanaka, Y. G. Ro, A. K. Matsushita, X. Dai, C. Soci, S. Biesmans, A. James, J. Nogan, K. L. Jungjohann, D. V. Pete, D. B. Webb, Y. Zou, A. G. Bang, S. A. Dayeh, *Nano Lett.* **2017**, *17*, 2757.
- [31] R. Liu, J. Lee, Y. Tchoe, D. Pre, A. M. Bourhis, A. D'Antonio-Chronowska, G. Robin, S. H. Lee, Y. G. Ro, R. Vatsyayan, K. J. Tonsfeldt, L. A. Hossain, M. L. Phipps, J. Yoo, J. Nogan, J. S. Martinez, K. A. Frazer, A. G. Bang, S. A. Dayeh, *Adv. Funct. Mater.* **2022**, *32*, 2108378.
- [32] Y. Cao, H. Chen, R. Qiu, M. Hanna, E. Ma, M. Hjort, A. Zhang, R. S. Lewis, J. C. Wu, N. A. Melosh, *Sci. Adv.* **2018**, *4*, eaat8131.
- [33] X. Xie, A. Aalipour, S. V. Gupta, N. A. Melosh, *ACS Nano* **2015**, *9*, 11667.
- [34] A. Czeschik, A. Offenhäusser, B. Wolfrum, *Phys. Status Solidi A* **2014**, *211*, 1462.
- [35] Y. Cao, M. Hjort, H. Chen, F. Birey, S. A. Leal-Ortiz, C. M. Han, J. G. Santiago, S. P. Pasca, J. C. Wu, N. A. Melosh, *Proc. Natl. Acad. Sci. USA* **2017**, *114*, E1866.
- [36] R. Tang, W. Pei, S. Chen, H. Zhao, Y. Chen, Y. Han, C. Wang, H. Chen, *Sci. China Inf. Sci.* **2014**, *57*, 1.
- [37] C. Boehler, T. Stieglitz, M. Asplund, *Biomaterials* **2015**, *67*, 346.
- [38] P. Yin, Y. Liu, L. Xiao, C. Zhang, *Polymers* **2021**, *13*, 2834.
- [39] J. D. Weiland, D. J. Anderson, M. S. Humayun, *IEEE Trans. Biomed. Eng.* **2002**, *49*, 1574.
- [40] S. Seyock, V. Maybeck, E. Scorsone, L. Rousseau, C. Hébert, G. Lissorgues, P. Bergonzo, A. Offenhäusser, *RSC Adv.* **2017**, *7*, 153.
- [41] C. Xie, L. Hanson, W. Xie, Z. Lin, B. Cui, Y. Cui, *Nano Lett.* **2010**, *10*, 4020.
- [42] A. Hai, J. Shappir, M. E. Spira, *J. Neurophysiol.* **2010**, *104*, 559.
- [43] L. Hanson, Z. C. Lin, C. Xie, Y. Cui, B. Cui, *Nano Lett.* **2012**, *12*, 5815.
- [44] H.-Y. Lou, W. Zhao, X. Li, L. Duan, A. Powers, M. Akamatsu, F. Santoro, A. F. McGuire, Y. Cui, D. G. Drubin, *Proc. Natl. Acad. Sci. USA* **2019**, *116*, 23143.
- [45] E. Tibau, M. Valencia, J. Soriano, *Front. Neural Circuits* **2013**, *7*, 199.
- [46] J. van Pelt, P. S. Wolters, M. A. Corner, W. L. Rutten, G. J. Ramakers, *IEEE Trans. Biomed. Eng.* **2004**, *51*, 2051.
- [47] J. Abbott, T. Ye, D. Ham, H. Park, *Acc. Chem. Res.* **2018**, *51*, 600.
- [48] Q. Qing, Z. Jiang, L. Xu, R. Gao, L. Mai, C. M. Lieber, *Nat. Nano-technol.* **2014**, *9*, 142.
- [49] K. Weir, O. Blanquie, W. Kilb, H. J. Luhmann, A. Sinning, *Front. Cell. Neurosci.* **2015**, *8*, 460.
- [50] J. R. Buitenweg, W. Rutten, W. Willems, J. W. van Nieuwkastele, *Med. Biol. Eng. Comput.* **1998**, *36*, 630.
- [51] W. G. Regehr, J. Pine, C. S. Cohan, M. D. Mischke, D. W. Tank, *J. Neurosci. Methods* **1989**, *30*, 91.
- [52] D. Braun, P. Fromherz, *Biophys. J.* **2004**, *87*, 1351.
- [53] G. Wrobel, R. Seifert, S. Ingebrandt, J. Enderlein, H. Ecken, A. Baumann, U. B. Kaupp, A. Offenhäusser, *Biophys. J.* **2005**, *89*, 3628.
- [54] C. R. Caro-Martín, J. M. Delgado-García, A. Gruart, R. Sánchez-Campusano, *Sci. Rep.* **2018**, *8*, 17796.
- [55] J. Abbott, T. Ye, K. Krennek, R. S. Gertner, W. Wu, H. S. Jung, D. Ham, H. Park, *Lab Chip* **2020**, *20*, 3239.
- [56] D. Jäckel, D. J. Bakkum, T. L. Russell, J. Müller, M. Radivojevic, U. Frey, F. Franke, A. Hierlemann, *Sci. Rep.* **2017**, *7*, 978.
- [57] J. Riedl, A. H. Crevenna, K. Kessenbrock, J. H. Yu, D. Neukirchen, M. Bista, F. Bradke, D. Jenne, T. A. Holak, Z. Werb, M. Sixt, R. Wedlich-Soldner, *Nat. Methods* **2008**, *5*, 605.
- [58] A. Belu, J. Schnitker, S. Bertazzo, E. Neumann, D. Mayer, A. Offenhäusser, F. Santoro, *J. Microsc.* **2016**, *263*, 78.